Inhalation Toxicology, 2010; 22(4): 287–300

informa
healthcare

RESEARCH ARTICLE

Inhalability of micron particles through the nose and mouth

Camby Mei King Se, Kiao Inthavong, and Jiyuan Tu

School of Aerospace, Mechanical and Manufacturing Engineering, RMIT University, Bundoora, Victoria, Australia

Abstract

Aspiration efficiencies from nose and mouth inhalations are investigated at low and high inhalation rates by using the commercial Computational Fluid Dynamics (CFD) software CFX 11. A realistic human head with detailed facial features was constructed. Facial features were matched to represent the 50th percentile of a human male, aged between 20 and 65 years old, based on anthropometric data. The constant freestream velocity was 0.2 ms^{-1}, normal to the face, and inhalation rates through the mouth and nose were 15 liters per minute (LPM) for light breathing and 40 LPM for heavy breathing. It was found that the flow field in the near breathing region exhibited vertical direction caused by the presence of the torso where the airstream diverges as it flows around and over the body. The critical area concept was used as a tool to determine the aspiration efficiency of particles. Comparisons between critical areas for the nose and mouth inhalations show similar geometric properties such as the area's shape, and its vertical distance location on the *x*-*z* plane located at $y = 80$ cm upstream. The critical area sizes were found to be slightly larger for the mouth inhalation mainly due to the larger mouth area and also the aligned orientation of the mouth to the upstream flow, whereas the nose is perpendicular to the upstream flow. This study was undertaken to establish the flow field in the near breathing region that will help to characterize the flow and particle field for initial boundary conditions leading to a more holistic modeling approach of respiration through the internal nasal cavity and mouth.

Keywords: *Aspiration efficiency; computational fluid dynamics; particle inhalability*

Introduction

Inhalation of toxic airborne contaminants such as asbestos, acid mist, smoke, and diesel fumes is a frequent occurrence for those working in the manufacturing and processing industries. In more recent times, the outbreak of viruses (SARS [severe acute respiratory syndrome], equine flu, swine flu, bird flu) is a consequence of the transportation of viral particles found in the airstreams. Although viruses usually exist on a nano scale, they are usually transported with water molecules from sneezing or coughing. The impact of inhaling such infected water-based particles has led to chaotic situations in 2004 for the outbreak of SARS and 2009 of the swine flu. Airborne particles enter the body through the nose or mouth, leading to deposition within the respiratory system, which in turn has many potential health risks. The respiratory system has its own physiological defensive reactions to the presence of airborne particulates. For example, high bifurcation angles in the lung airways, mucociliary action in ciliated wall regions that trap and remove the particles, and 90° curvatures in the airway geometry found at the nostril inlet, at the nasopharynx, and at the oropharynx. Despite these natural defences, airborne particulates, especially low-Stokes-numbered particles and nano-scaled particles, often become entrained in the airflow and deposit deep into the respiratory system, causing serious health problems. Studies of deposition in the respiratory system have been previously studied by the authors (Inthavong et al., 2008a, 2008b), among other researchers (Balashazy et al., 2003; Crowder et al., 2002; Kleinstreuer & Zhang 2003). These studies were exclusively limited to the internal respiratory system (nose and lung airways).

In contrast, micron particles tend to deposit in the nasal cavity. Deposition efficiency in the nasal cavity under different inhalation flow rates has been extensively

Address for Correspondence: Prof. Jiyuan Tu, School of Aerospace, Mechanical and Manufacturing Engineering, RMIT University, PO Box 71, Bundoora Vic 3083, Australia. Tel: +61-3-9925 6191; Fax: +61-3-9925 6108; E-mail: jiyuan.tu@rmit.edu.au

(Received 30 July 2009; revised 27 August 2009; accepted 28 August 2009)

ISSN 0895-8378 print/ISSN 1091-7691 online © 2010 Informa UK Ltd
DOI: 10.3109/08958370903295204

investigated (Inthavong, 2006; Inthavong et al., 2006, 2009b; Shi et al., 2008; Guilmette et al., 1994; Zwartz & Guilmette 2001). However, external conditions, such as airflow field, and particle inhalability were not considered in any particular detail. For example, the inhalation of wood dust through the nasal cavity was simulated (Tian et al., 2007) by injecting particles from a particle size distribution defined from settled particles on the ground (Chung et al., 2000) rather than a particle size distribution (PSD) suspended in the breathing region of the worker. With this consideration, the inhalable PSD can be defined that presents a more realistic initial boundary condition for future deposition studies in the respiratory system. Applying such experimental PSD neglects the impact of inhalation and the surrounding freestream airflow on particle inhalation through the mouth or nose. Through an integrated modeling approach presented in this study, the results will contribute towards a more realistic model for inhalation and toxicological studies.

Therefore in this study, Computational Fluid Dynamics (CFD) modeling is used to visualize and compare the effects of nose and mouth inhalations of airborne particles. The inhalability of airborne particles from a contaminant source upstream is evaluated to determine the risk it can pose to a person exposed to the particles. A three-dimensional humanoid was created with emphasis on realistic facial features that included detailed mouth and nose. A holistic approach incorporating the external environment such as the flow field and contaminant source, coupled with human factors that include the humanoid body shape, facial features, and inhalation through the nose and mouth, are considered. Results such as the aspiration efficiency can be quantified, which provides the basis of initial boundary conditions for internal nasal cavity and lung airway particle deposition studies.

Aspiration efficiency

Particle inhalability or aspiration efficiency has been measured as the fraction of particles that are inhaled through the nose or mouth during breathing (Vincent, 1999). Based on the experimental studies by Vincent and Mark (1982), Ogden and Birkett (1977), and Armbruster and Breuer (1982), a sampling criterion for the Inhalable Particulate Matter (IPM) of orientation-averaged mouth inhalation and wind speed of 0.4 ms^{-1} or below was developed:

$$\mathrm{IPM} = 0.5\left(1+\exp\left(-0.06 d_{ae}\right)\right),\ d_{ae} \le 100\,\mu\mathrm{m} \quad (1)$$

where d_{ae} is the aerodynamic diameter of the particle. The inhalability measurements made by Ogden and Birkett (1977) and Armbruster and Breuer (1982) used a mannequin head with inhalation only, whereas those made by Vincent and Mark (1982) used a mannequin that inhaled through the mouth and exhaled through the nose. Comparisons of these results do not show any detectable differences in the results that can be attributed to the exhalation pattern. It is important to note that the IPM curve is limited to wind velocities between 1 and 4 m/s, particles with aerodynamic diameters no larger than 100 µm (due to the requirement of maintaining uniform concentrations of large aerosols), orientation averaged, and for mouth inhalation only. These limitations make the IPM curve lack generality and does not allow for direct applications to different conditions such as the nasal breathing or lower environmental wind speeds. The difficulties in obtaining a uniform suspension of large particles at low velocities, and the costs associated with experimental studies performed in large wind tunnels have lead to CFD simulations as an alternative. Early studies began with simple geometric shapes acting as surrogates for the human body. For example Ingham and Hildyard (1991) used an infinitely long cylinder to represent the body, Erdal and Esmen (1995) used a hemispherical top for the head placed on a cylinder that represented the body, and Hyun and Kleinstreuer (2001) used a sphere as the head of mannequin. In all cases, an oval opening was used to represent the "mouth" of the surrogate bodies. Studies by Anthony et al. (2005) found that using simplified body and facial features was inadequate. In their study, a mannequin with detailed facial features was compared with a cylindrical human form having an oval opening for the mouth. It was found that a cylindrical form inhaled more particles through the mouth when compared to an adult-size mannequin, particularly for facing-the-wind orientation. Inhalation through the nose was not studied. It was also found that the aspiration efficiency decreased due to the projection of the anatomical mannequin's facial features in front of the mouth opening. Facial features resulted in a reduction of the horizontal velocity upstream from the nose, although this was limited to 10 mm in front of the nose tip. Similar findings were also obtained in a study on an child-size mannequin undertaken by Heist et al. (2003).

Methods

Geometric modeling

In this study, a realistic human head was generated as an IGES file from FaceGEN Modeller (Singularity Inversion Inc., 2007) software, based on photographic images taken from a male volunteer. The three-dimensional (3D) head contained detailed facial features, such as shaped eyes, nose, mouth, and ears. The IGES file contained the surface and volume information, which was then exported into ICEM CFD (Ansys Inc., 2007) for CFD mesh construction (Figure 1). Slight modifications were made to the computational model where possible, to allow the model dimensions to represent the 50th percentile of a human male, aged between 20 and 65 years old, based on anthropometric data of Tilley (1993) (see Table 1). The opening of the mouth has maximum dimensions of 2 cm wide and 0.5 cm high, resulting in a total area of 5.49 cm^2, which compares with 2.2 cm^2 in Dunnet and Ingham (1988) and 7.1 cm^2 in Hsu and Swiftt (1999).

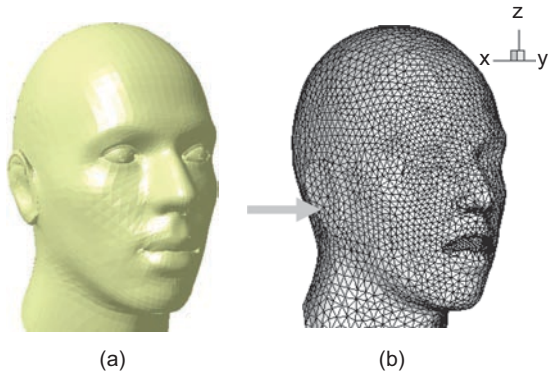

Figure 1. Computer model generated from (a) raw IGES file created from FaceGEN Modeller (Singularity Inversion Inc., 2007) and (b) meshed face constructed in ICEM CFD (Ansys Inc., 2007).

Table 1. Dimension of the humanoid.

Dimension	Present study	50th percentile man
Head (cm)		
Head width	14.0	15.5
Head depth	20.0	19.6
Top of head to chin	23.0	22.1
Location of mouth center, relative to the top of head	17.3	18.0
Mouth (cm)		
Horizontal axis	5.1	5.1
Vertical axis	1.2	1.0–2.2
Equivalent diameter	1.322	—
Hydraulic radius	0.987	—
Mouth area (cm^2)	5.49	2.2*–7.1**

Note. Data from *Dunnet and Ingham (1988), **Hsu and Swiftt (1999).

Unstructured tetrahedral mesh is adopted with a fine mesh around the mouth, nostril, and high irregular and complex regions. Anthony and Flynn (2006a) showed that truncating the full body at the hips produced vertical velocity components that were consistently smaller than experimental validation. Thus, a full-scale body at 1.7 m tall was attached to the 3D head generated from FaceGEN Modeller and the full-bodied model was placed in a tunnel with dimensions of 4 m wide × 10 m deep × 3 m high (Figure 2). The dimensions of the wind tunnel were created large enough so the flow field near the humanoid was free from the effects of the no-slip condition of the stationary surrounding walls.

Fluid flow modeling

A steady freestream velocity was applied at the inlet while at the outlet a zero-pressure gradient boundary condition was used. A comprehensive survey of airflow speeds in indoor workplaces by Baldwin and Maynard (1993) found a mean value of 0.3 ms^{-1}. The freestream velocity direction is normal to the facial features, which is referred to as 'facing-the-wind' flow direction. Reynolds number matching over the head of the humanoid was applied in order to obtain dynamic similarity between the present numerical study with the experimental data found in the literature (Anthony et al., 2005). Similarly, the inhalation conditions through the mouth were also matched by the Reynolds number (see Table 2). Two inhalation rates of 15 and 40 liters per minute (LPM) were studied for the aspiration efficiency through nasal and oral inhalation see Table 3, which represent light activity and heavy

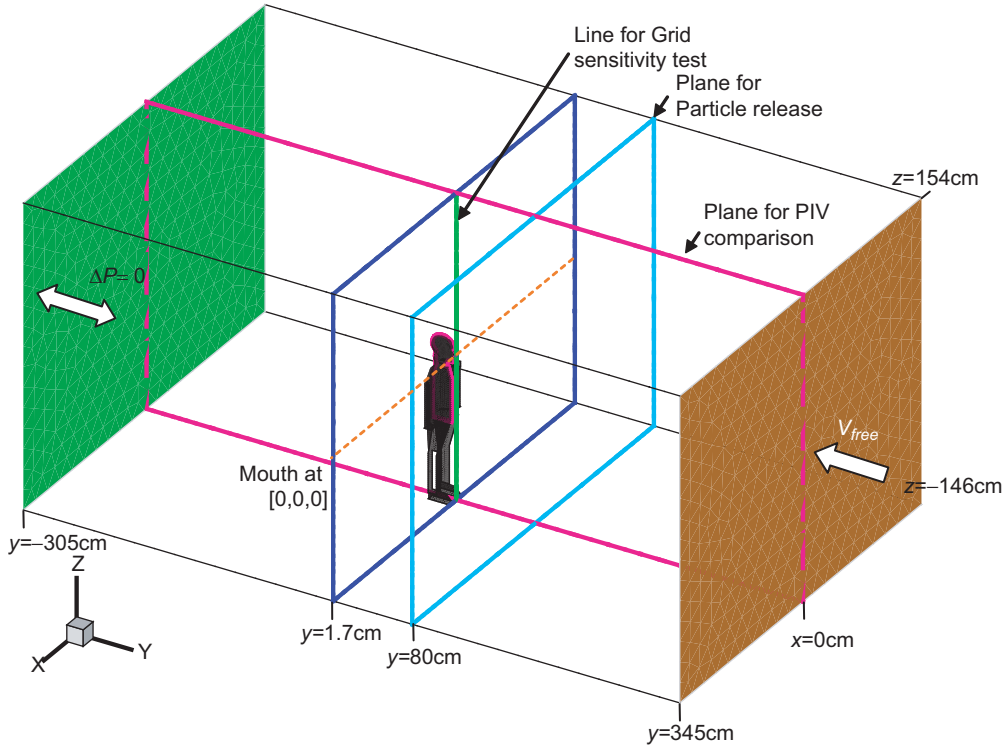

Figure 2. Layout of the computational domain.

Table 2. Dynamic similarity matching for the present study with the study of Anthony et al. (2005).

Dimension	Anthony et al. (2005)	Present study
$Re_{freestream}$	1909	1909
Characteristic length (cm) (head hydraulic diameter)	9.6	14.0
V_{free} (ms^{-1})	0.30	0.20
Re_{inhale}	1590	1590
Characteristic length (cm) (mouth equivalent diameter)	8.87	9.87
Mouth area (cm^2)	0.618×10^{-4}	5.49×10^{-4}
Inhalation velocity (ms^{-1})	2.700	1.816

Table 3. Inhaling mass flow rate for each scenario.

	Nasal inhalation*		Oral inhalation	
	15 LPM	40 LPM	15 LPM	40 LPM
Inhaling mass flow rate (E-4 m^{3}s^{-1})	4.97	13.33	4.97	13.33

*Assume the inhalation velocity through each nostril shares equally.

Table 4. Aspiration efficiency for various inhalation rates against different particle sizes.

		Aspiration efficiency, AE						
Inhalation		1 μm	5 μm	10 μm	20 μm	40 μm	80 μm	140 μm
Nasal	15 LPM	0.86	0.81	0.80	0.78	0.77	0.70	0.00
	40 LPM	0.85	0.83	0.82	0.81	0.78	0.62	0.00
Oral	15 LPM	0.89	0.89	0.89	0.88	0.88	0.80	0.00
	40 LPM	0.92	0.91	0.87	0.83	0.83	0.78	0.00

exertion in the workplace environment, respectively (Snyer, 1975). Assuming inhalation and exhalation times are shared equally during an inhalation cycle, these two inhalation rates correspond to tidal volumes of about 500 and 1200 L, respectively.

The inlet velocity corresponds to Re_{inlet} = 16,433 at the inlet. The modeling assumptions applied for the CFD simulations include fully turbulent isothermal, incompressible flow. The isothermal assumption was used to allow direct velocity profile comparisons with the experimental data of Anthony et al. (2005), which used a mannequin without any heat flux. The *k-ε* turbulence model, which is a robust, low computational cost model, has been widely used in 3D simulations of personal exposure to contaminant sources in ventilated rooms (Brohus & Nielsen, 1996; Brohus, 1997; Zhu et al., 2005). However, the standard *k-ε* model is a poor predictor of flow separation (Durbin, 1995). The Re-Normalisation Group (RNG) *k-ε* model used in Hyun and Kleinstreuer (2001) and Bird (2005) for the simulation of inhaled indoor pollutants is also used in this study. In addition, reported results have shown much better flow separation and reattachment for the RNG *k-ε* model (Speziale & Thangam, 1992), which is an expected flow feature of the flow passing over the head.

The steady, incompressible turbulent Navier-Stokes equations were used to model the airflow. The continuity and momentum equations are given in Equations (2) and (3), respectively.

$$\nabla\cdot\left(\rho\vec{U}\right)=0 \tag{2}$$

$$\nabla\cdot\left(\rho\vec{U}\otimes\vec{U}\right)=\nabla\cdot\left(\mu+\mu_t\right)\left(\nabla\vec{U}+\left(\nabla\vec{U}\right)^T-\frac{2}{3}\delta_{ij}\nabla\cdot\vec{U}\right)-\nabla p \tag{3}$$

where $\mu_t=\rho c_\mu k^2/\varepsilon$ and δ_{ij} is the Kronecker delta, $\delta_{ij}=1$ if $i=j$ and $\delta_{ij}=0$ if $i\neq j$.

The RNG *k-ε* model equations can be cast in Equation (4) and (5).

$$\nabla\cdot\left(\rho\vec{U}k\right)=\nabla\cdot\left[\left(\mu+\frac{\mu_t}{\sigma_k}\right)\nabla k\right]+\mathrm{P}_k-\rho\epsilon \tag{4}$$

$$\nabla\cdot\left(\rho\vec{U}\epsilon\right)=\nabla\cdot\left[\left(\mu+\frac{\mu_t}{\sigma_{\epsilon RNG}}\right)\nabla\epsilon\right]+\frac{\epsilon}{k}\left(C_{\epsilon1RNG}P_k-C_{\epsilon2RNG}\rho\epsilon\right) \tag{5}$$

where $P_k=\mu_t\nabla\vec{U}\cdot\left(\nabla\vec{U}+\nabla\vec{U}^T\right)-\frac{2}{3}\nabla\cdot\vec{U}\left(3\mu_t\nabla\cdot\vec{U}\right)+\rho k+\mathrm{P}_{kb}$

$c_\mu=0.09$, $\sigma_k=1.00$, $\sigma_{\epsilon RNG}=1.30$, $C_{\epsilon2RNG}=1.92$,

$C_{\epsilon1RMG}=1.42-\mathrm{f}_\eta$, in which

$$f_\eta=\frac{\eta\left(1-\frac{\eta}{4.38}\right)}{\left(1+\beta_{RNG}\eta^3\right)} \text{ and } \eta=\sqrt{\frac{P_k}{\rho C_{\mu RNG}\epsilon}}$$

To resolve the boundary layer in the near wall regions, the Scalable Wall Function (Menter & Esch 2001) was used. The fluid flow equations (Equations 2–5) were solved in ANSYS CFX v11.0 using a segregated solver with an implicit formulation. The pressure-velocity coupling was resolved by the SIMPLEC algorithm. The convective terms of the transport equations were all discretised using second-order-upwind scheme in order to obtain sufficiently accurate solutions. In addition, the residual values of the governing equations and the transport equations were all set to converge at 10^{-5} or below for all simulation cases.

Particle phase modeling

Individual representative particles are tracked separately through the flow field in a Lagrangian approach. The equation of motion for each particle is given in Equation (6):

$$m_P\frac{du_P}{dt}=F_D+F_B+S_i \tag{6}$$

where m_i^p is the mass of particle, $m_P=\frac{\pi}{6}d_P^3\rho_P$, and A_F is the effective cross section.

The drag force acting on the particle, F_D, is given by

$$F_D=\frac{1}{2}C_D\rho_F A_F\left|U_F-U_P\right|\left(U_F-U_P\right) \tag{7}$$

whereas the buoyancy force due to gravity, F_B, is given as

$$F_B = (m_P - m_F)g \tag{8}$$

where U_F, U_P, ρ_F, and ρ_P are fluid (air) velocity, particle velocity, fluid density, and particle density, respectively.

The drag coefficient, C_D, is evaluated from an experimental-fitted expression given by Schiller and Naumann (1933) in Equation (9), which considered the limiting behavior in the inertial regime.

$$C_D = \max\left(\frac{24}{\mathrm{Re}}\left(1+0.15\mathrm{Re}_p^{\,0.687}\right), 0.44\right) \tag{9}$$

where the Reynolds number of particle is defined as Equation (10)

$$\mathrm{Re}_p = \frac{\rho_a \left| v_{fluid} - v_p \right| d_{ae}}{\mu} \tag{10}$$

The new particle velocity is then calculated by using Equation (11), which is the analytical solution to Equation (6).

$$u_p = u_{fluid} + \left(u_p^{old} + u_{fluid}\right)\exp\left(-\frac{\delta t}{\tau_p}\right) + \tau F_T\left(1-\exp\left(-\frac{\delta t}{\tau_p}\right)\right) \tag{11}$$

where $\tau_p = \rho_p d_p^2 / 18\mu_g$, which is the particle relaxation time and F_T is the total force.

The particle displacement is calculated using forward Euler integration in Equation (10), of the particle velocity u_{pi}^{old}, over a timestep δt.

$$x_i^{new} = x_i^{old} + u_{pi}^{old}\,\delta t \tag{12}$$

In the forward integration, the particle velocity calculated at the start of the timestep is assumed to prevail over the entire step. At the end of the timestep, the new particle velocity is taken from Equation (11).

One-way coupling is assumed between the air and particle flow fields and the interaction between particles is also neglected because the particle flow is dilute (i.e., the volume fraction of the particles is less than 10%). S_i is the additional forces that may include the rotation force, pressure gradient force, virtual mass effect, and Basset force. Contaminant aerosols in the micron size range such as acid mist, asbestos, and wood dust are typically far denser than air, causing terms that depend on the density ratio, such as those in S_i, to be negligibly small. The turbulent dispersion of the particle tracking is modeled through the eddy interaction model where the particle is assumed to be always within a single turbulent eddy and each eddy has a characteristic fluctuating velocity u'_P, lifetime τ_e and length l_e. The fluctuating velocity for that eddy is added to the local mean fluid velocity in Equation (11) to obtain the instantaneous fluid velocity. The turbulence scales are defined as

$$u'_P = \Gamma\sqrt{2k/3} \tag{13}$$

$$l_e = \frac{C_\mu^{3/4}}{\epsilon}k^{3/2} \tag{14}$$

$$\tau_e = \frac{l_e}{\sqrt{2k/3}} \tag{15}$$

where Γ is a normally distributed random number, and k is the local turbulent kinetic energy. Further details of the model is found in the ANSYS CFX documentation (Ansys Inc., 2006).

Inhalability and critical area

The aspiration efficiency is defined as the ratio of the inhaled particle concentration (C) to the ambient freestream particle concentration (C_o)

$$AE = C/C_o \tag{16}$$

The inhaled concentration, C, can be expressed as the number of particles inhaled (N_n) per volume, $A_n V_n t$,

$$C = \frac{N_n}{A_n V_n t} \tag{17}$$

where A_n is the inhalation area, V_n is the average inhalation velocity, and t is the time.

Experimental and numerical studies assume a uniform particle concentration upstream of the humanoid, because the velocity field is unaffected by the presence of the person. Over any upstream cross-sectional area, the particle concentration is the ratio of the number of particles in the freestream, N_C, to the volume of air through the cross-sectional area, which is the product of the cross-sectional area (A_C), the average velocity through the cross-section (V_C), and time (t):

$$C_O = \frac{N_C}{A_C V_C t} \tag{18}$$

The aspiration efficiency is evaluated based on the particles that are actually inhaled, which obviates the need simulate particle releases that are uniformly distributed across the entire inlet. The original locations of the inhaled particles can be determined by looking up the particle statistics from the Lagrangian tracking. A map can then be created on the release (x-z plane at y = 80 cm) showing only the particles that are inhaled, and the enclosed region forms the cross-sectional area A_C. A_C is termed the critical area in Anthony and Flynn (2006b), which represents a region

of inhalable particles upstream from the humanoid. By applying the critical area concept $N_C = N_n$, the aspiration efficiency becomes

$$AE = \frac{A_C V_C}{A_n V_n} \tag{19}$$

Grid and particle number independence

The generated mesh surrounding the body was gradually made coarse toward the surrounding walls. Grid refinements at surfaces, and the level of coarsening towards the walls, were changed to increase the number of cells in the model. Three different models of 480,000, 1.2 million, and 2.6 million cells were created and tested for grid independence through velocity profiles taken along a line at x = 0 cm, y = 1.7 cm, upstream of the mouth in the x-z plane, which cuts through the centerline of the humanoid (Figure 3). The grid was considered converged for 1.2 million cells where velocities along a profile exhibited <0.5% change when the mesh was increased to 2.6 million cells. Particles were introduced into the computational domain along the x-z plane at y = 80 cm upstream (Figure 2), which satisfies the criteria that the point source has to be located at least four head diameters upstream of the humanoid to ensure negligible bluff-body effects on the freestream (Chung et al., 1997).

The number of particles tracked was checked for statistical independence because the turbulent dispersion is modeled based on a stochastic process. This was determined by repeated simulations where the number of particles was increased until the inhalation efficiency became independent of the number of particles. Independence was achieved for 30,000 particles because an increase of particles to 50,000 particles yielded a difference of 0.1% in the inhalation efficiency. To achieve the uniform particle concentration assumption, particles were released at the same velocity as the freestream.

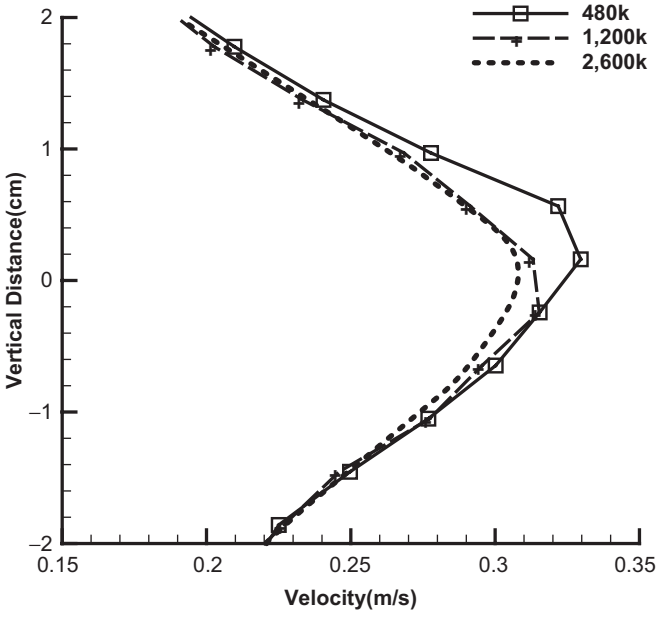

Figure 3. Velocity profiles for different grid convergence taken along the line 17 cm in front of the mannequin's face as shown in Figure 2. The Vertical Distance (cm) axis is 0 at the mouth opening.

Results and discussion

Validation through velocity vectors in the breathing region

Velocity vectors in the y-z plane at the centreline of the humanoid (x = 0 cm) are compared with the experimental data reported by Anthony et al. (2005) and shown in Figure 4. The Particle Image Velocimetry (PIV) data show black arrows that correspond to the flow field associated with a mannequin exhibiting realistic facial features, superimposed onto grey arrows, which correspond to the flow field from a simplified cylindrical human form. The flow field in the near breathing region shows slight vertical direction caused by the presence of the torso where the airstream diverges as it flows past the body. For mouth inhalation, vectors that are directed downwards towards the mouth occur earlier (y = 1.0 cm) in the horizontal plane for the CFD model and the realistic facial feature model in comparison with the cylindrical human form (y = 0.5 cm). Locally, the oncoming airflow bifurcates at the nose tip as well as at the chin. Downwards flow is found in the philtrum (space between the nose and the upper lip). In contrast, the same flow for nose inhalation is directed upwards towards the nostril openings. The effect of the vertical flow across the closed mouth region can enhance the inhalability of the particles if breathing through the mouth was to occur midway through a breath taken through the nose. Such case studies involving both the nose and mouth inhalations under different breathing situations were not investigated in this paper but would be interesting for future studies. The other flow difference found between mouth inhalation and nose inhalation is the higher stagnation point (flow bifurcation) near the chin for the nose inhalation.

Comparisons of the velocity profiles from the vector plots in Figure 4a and b in the near breathing regions at y = 1.0 cm (the nose tip) and y = 1.5 cm are shown in Figure 5. There is good agreement between the profiles, especially at y = 1.5 cm. Minimum velocities near the stagnation point at the nose tip height is found at the vertical distance of z = 2.0 cm for both cases. Maximum velocities occurs at the mouth at z = 0 cm and just below the mouth region where the flow accelerates from the chin region. Slight differences are found in the chin region below the lower lip and also in the philtrum, which may be attributed to some differences in the exact facial features.

Particle trajectories

Trajectories of the inhaled particles (Figure 6) show the influence of the inhalation and bluff body effects in the near breathing region. Only mouth inhalation is shown because the trajectories for the nose inhalation are similar and are left out for brevity. The trajectories

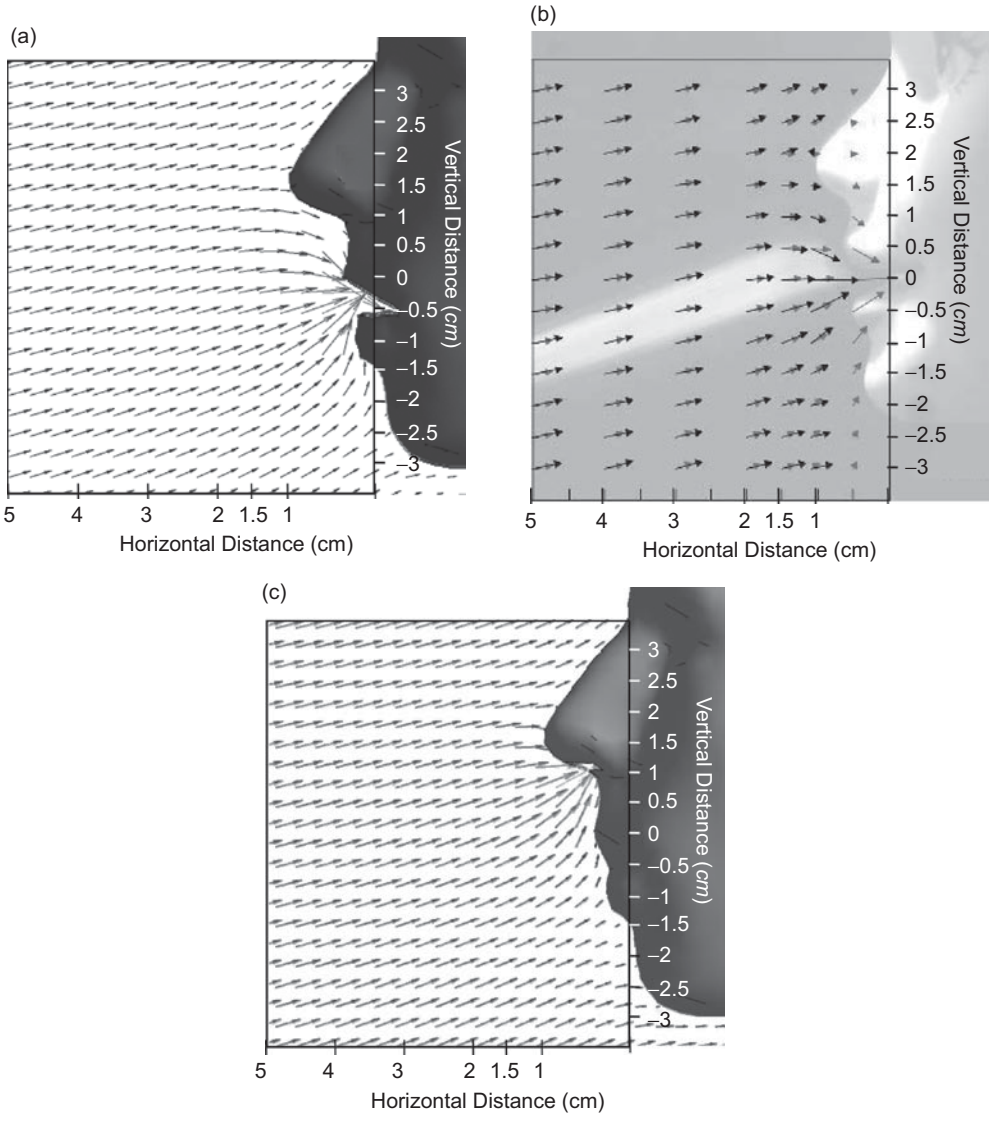

Figure 4. Velocity vector plots for (a) CFD oral inhalation and (b) PIV experimental measurements from Anthony et al. (2005). (c) CFD nasal inhalation.

show the larger streamtubes for the inhalation rate of 40 LPM, which are apparent from the increase in the critical inhalation areas found in Figure 7. The entrained 1-μm particle follows the lifting upstream flow field where the location of the critical area is below the mouth in the vertical direction. Particles within the inhaled streamtubes approaching the mouth are accelerated and depart from the flow field due to the mouth inhalation, eventually exiting through the mouth. The particle sizes of 80 and 140 μm, which are significantly affected by gravitational settling, show trajectories originating much higher vertically in relation to the mouth. The trajectory of the particles is linear until they reach the mouth inhalation where acceleration towards the mouth occurs. This linearity means that the location of the critical area for large particles can be easily identified for a given upstream distance. The further upstream the distance, the higher the vertical distance needs to be for the particles to descend towards the mouth. Particles that lay just outside of the streamtubes that did not get inhaled were impacted on the face and their trajectory ceased. Therefore any particle bounce that may occur with solid particulates was not considered in this study.

Critical areas and particle inhalation

The inhalability of particles with aerodynamic diameters of 1, 5, 10, 20, 40, and 80 μm released 80 cm upstream of the humanoid were studied in a facing-the-wind scenario. There were four cases that involved nasal and oral inhalation for the two inhalation rates of 15 and 40 LPM.

Figure 7 and Figure 8 show critical areas for all the particles on one graph, which was only possible by compressing the 'Vertical Distance (cm)' axis. It can be seen for all cases that gravitational settling becomes dominant for 40- and 80-μm particles, where the critical areas are located above the mouth position of $z = 0$ cm. In contrast, the vertical distances for the 1–10-μm particles are found at similar locations at $0 < z < 15$ cm, which is

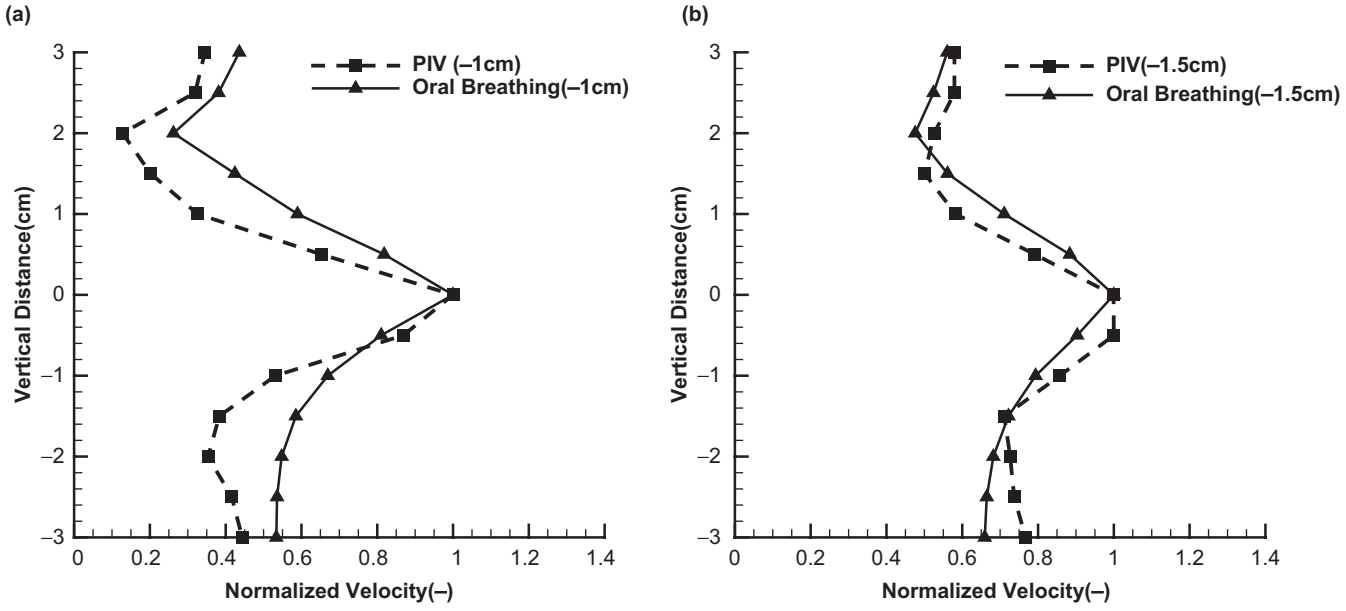

Figure 5. Velocity between the PIV measurements and the numerical results at (a) y = 1 cm from the mouth and (b) y = 1.5 cm from the mouth at the midsagittal plane (x = 0 cm).

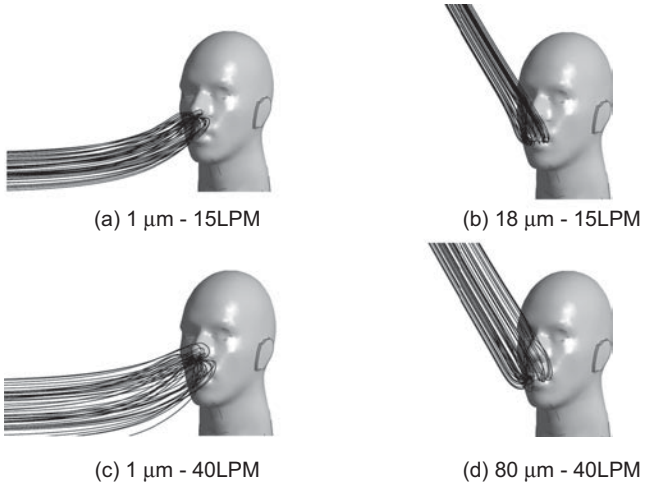

Figure 6. Trajectory of inhaled particles released at y = 80 cm upstream for 1-μm and 80-μm particles for mouth inhalation.

actually below the mouth location. This implies that the smaller particles are entrained and dependent on the flow field where the velocity vectors in Figure 4 show an upward flow in the near breathing region caused by flow separation as it passes over the humanoid. In this study, there is an absence of any additional ventilation system and the facing-the-wind scenario flow field is a horizontal flow defined by the inlet-outlet conditions. It can be imagined that in more realistic conditions where the flow field may not necessarily be a horizontal flow but contain low-velocity recirculation, flow separation, and wake flows, entrained small particles become more hazardous as they float through the open spaces and exhibit longer residence times. This leads to greater exposure to the harmful particles for the occupant and a greater reliance on local and general ventilation is needed for smaller particles. Larger particles become less dangerous because inhalation will only occur when the contaminant source is located above the humanoid, up to z = 70 cm above the mouth.

Comparisons between critical areas for the nose and mouth inhalations show similar geometric properties such as the teardrop shape, and its vertical distance location on the x-z plane located at y = 80 cm upstream. This similarity may be attributed to the normalization of inhalation velocities for the nose and mouth in order to achieve equal volume flow rates of 15 and 40 LPM. The critical area sizes are found to be slightly larger for the mouth inhalation, mainly due to the larger mouth area and also the aligned orientation of the mouth to the upstream flow, whereas the nose is perpendicular to the upstream flow. The flow field directly in the breathing region is influenced more by the higher inhalation rate of the nose, but this effect is in turn hindered by the smaller cross-sectional area of the nostrils and even further affected by the nostril's perpendicular alignment in relation to the flow field. The vertical alignment of the nostrils is an anatomical feature of the nose that can be thought of as an evolutionary defence mechanism that reduces the ability to inhale larger diameter airborne particles.

Comparisons between inhalation rates show an increase in the critical areas with increasing inhalation rates. The width of the critical area nearly doubles in size. An increase in the critical area height is also found but this is not as significant as the width increase, especially for the smaller particles where the gravitational settling is not significant. Whereas the trajectory of the particle is derived from the force balance in Equation (6), the potential for the particle to be entrained in the flow field can be

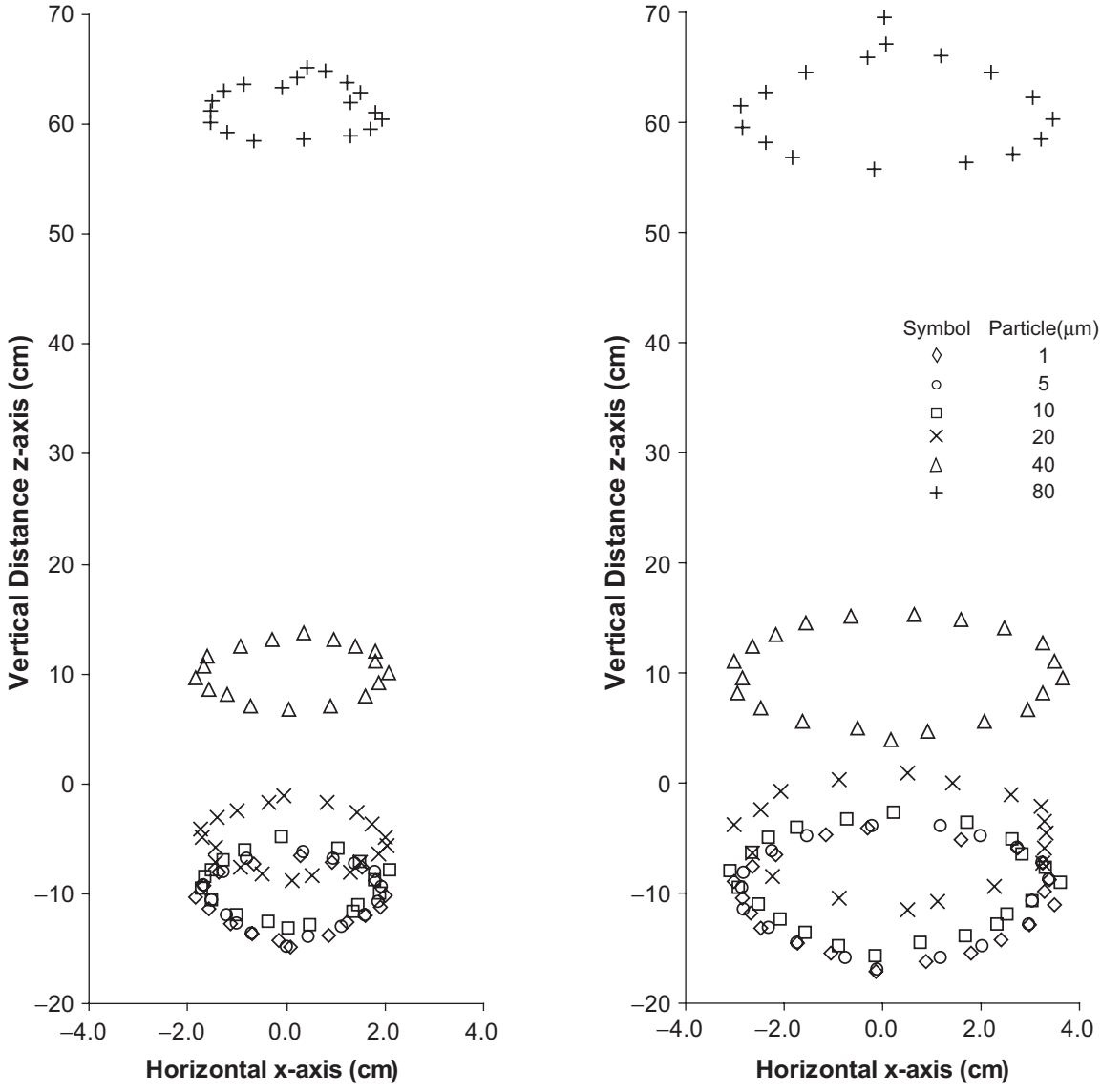

Figure 7. Scaled critical areas for different particle sizes for mouth inhalation at (a) 15 LPM and (b) 40 LPM.

determined through the particle Stokes number, which is the ratio of the particle relaxation time τ_p to the system response time τ_s:

$$St = \frac{\tau_p}{\tau_s} = \frac{\rho_p d_p^2}{18\mu_g}\frac{D}{U} \tag{20}$$

The increase in inhalation and therefore U in Equation (20) leads to an increase in the system response time. This reduces the particle Stokes number and enhances the likelihood of the particle to entrain in the inhaled flow streamlines.

Uncompressed critical areas for 1- and 80-μm particles are shown in Figure 9, which reveals the true shape of the upstream inhalable contaminant source. The two contrasting particle sizes are shown to reflect the influence of the particle Stokes number and gravitational settling under the higher inhalation rate of 40 LPM. Both critical areas for 1- and 80-μm particles resemble a teardrop shape but opposite in their vertical orientation. For 1-μm particles, the critical area is located below the nostril openings at z = 1.5 cm, where the thicker end of the teardrop shape is at the top. Gravitational settling is insignificant for the 1-μm particle and its flight path is dependent on the flow field, which is slightly directed upwards as seen in the vector plots of Figure 4. For 80-μm particles, the effect of the low indoor velocity flow field is less significant whereas the gravitational settling becomes important. As a result, the vertical distance of the critical area is relatively higher, reaching up to z = 70 cm above the mouth opening. The teardrop shape of the critical area has the thicker end at the bottom where the majority of the particles are transported across the flow field 80 cm horizontally and 70 cm downwards towards the nostril openings. With heavier particles, the contaminant source location needs to be even higher for the same horizontal distance away from the humanoid. The authors also simulated 140-μm

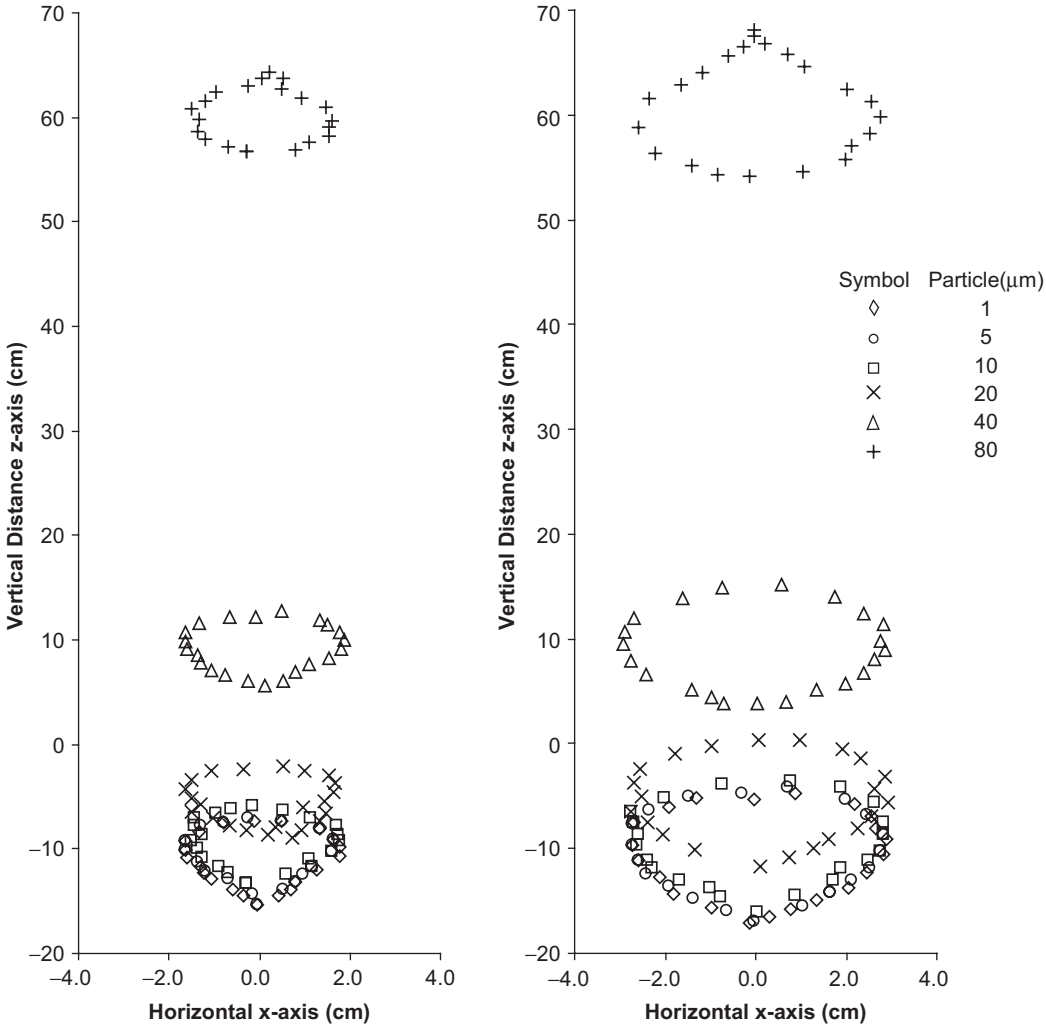

Figure 8. Scaled critical areas for different particle sizes for nose inhalation at (a) 15 LPM and (b) 40 LPM.

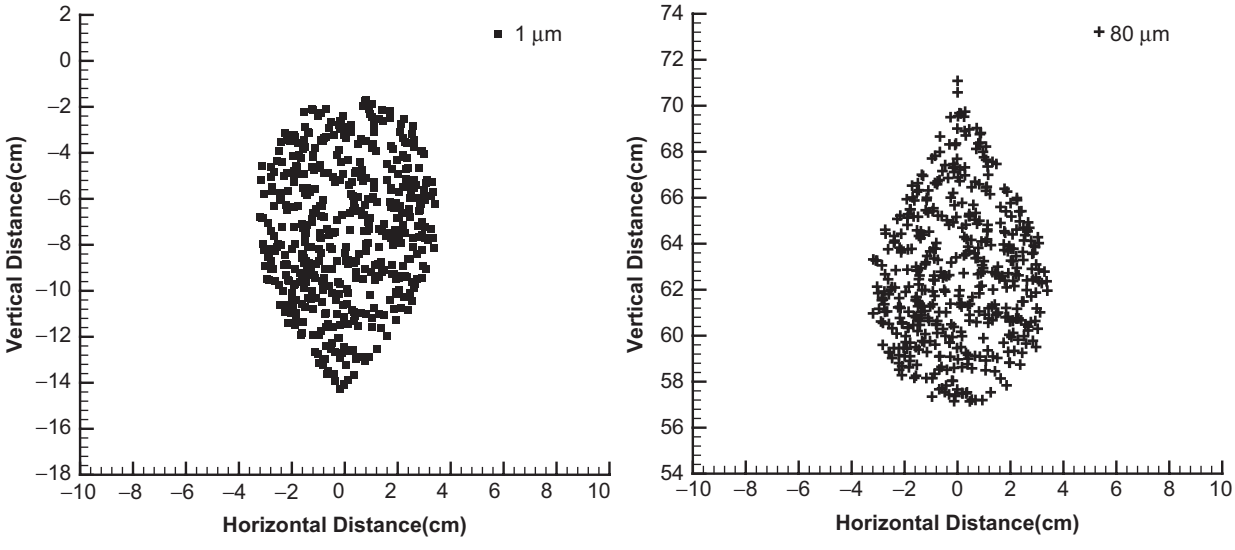

Figure 9. Uncompressed critical area of nose inhalation at 40 LPM for particle sizes of 1 μm and 80 μm.

particles to test this idea, which found that from the same release plane, no particles reached the humanoid. Instead, gravitational settling became dominant for the 140-μm particles, which forced the particles to fall to the ground much earlier. Further testing found that for inhalation to occur, the 140-μm particles had to be released at $y = 65$ cm or approximately five head diameters upstream of the humanoid.

Aspiration efficiency

The aspiration efficiency (AE) for facing-the-wind orientation for mouth inhalation is given in Figure 10 as well as Table 4, which shows a general decrease of AE with increasing particle size. Increased inhalation from 15LPM to 40LPM produced an increase in the AE. The 140-µm particles were also included but no particles were inhaled when released from the upstream distance of y = 80 cm at a mouth inhalation rate of 15 LPM. The results are based on the assumption that the particle contaminant source is within the computational domain vertical height, which is z = 154 cm above the mouth, and the release point located at y = 80 cm. If the vertical height within the computational domain was to extend further, it was thought that the 140-µm particles would be able to achieve some inhalation. The authors tested shorter upstream distances and found that no inhalation occurred for the 140-µm particles even at a very close distance of y = 10 cm.

Comparisons of the aspiration efficiency are made with Kennedy and Hinds (2002) and Anthony and Flynn (2006b). Additional comparisons with the orientation average were not made, as the CFD results are aimed at investigating the worst-case scenario. In the application of the AE results for risk management, the worst-case scenario must be used and to account for variabilities. Furthermore, factors of safety should be further applied when setting safety measures such as worker exposure limits and design and layout of workspace. The comparisons with the experimental data of Kennedy and Hinds (2002) show a underprediction for smaller particles. The experimental data used realistic breathing conditions for a tidal volume inhalation of 20 LPM, which produces a peak velocity much greater than an averaged steady flow. The higher peak velocity leads to an increase in the smaller particle AE.

Comparisons with the numerical data of Anthony and Flynn (2006b) also show an underprediction; however, both have similar profiles. The AE does not change greatly for aerodynamic diameters between 1 and 70 µm, but a large drop in the AE is found for aerodynamic diameters greater than 70 µm. The numerical data from Anthony and Flynn (2006b) were also obtained under a steady-state inhalation, whereas the established IPM curve has been established from unsteady breathing with an orientation average, only tested under freestream velocities between 1 and 4 ms^{-1}. Therefore for lower freestream velocities, which are common in indoor environments, the IPM curve may not be suitable as a tool for determining the risk of particle inhalation.

The only recorded AE for nose inhalation is from the work of Kennedy and Hinds (2002), which is used to compare the numerical results of this paper (Figure 11). The AE trend is similar to the numerical results for the mouth inhalation where the AE does not change greatly for aerodynamic diameters between 1 and 70 µm, but a large drop in the AE is found for aerodynamic diameters greater than 70 µm. In the experimental work of Kennedy and Hinds (2002), nose inhalability drops from nearly 100% for 7-µm particles to less than 10% for particles between 50 and 80 µm. The inhalability for particles larger than 80 µm increases, but this trend is thought to be unclear in the experiment because of large variabilities. There are some differences between the numerical results and the experimental data. For particle size between 1 and 70 µm, the higher peak velocity from unsteady inhalation leads to an increase in the AE. This effect is not significant for larger particles, which are prone to gravitational settling. It was shown in the particle trajectories section that the contaminant source of larger particles needed to be above the inhalation region due to gravitational settling and for larger particles a minimum height was needed in order to achieve any particle inhalation. The experimental of Kennedy and Hinds (2002) set up the aerosol delivery

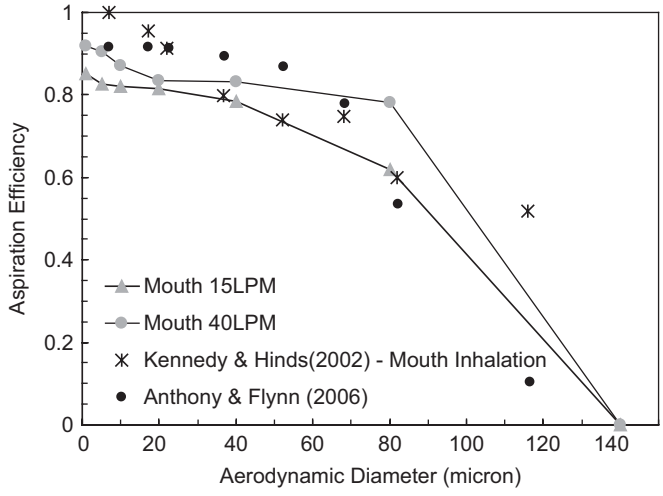

Figure 10. Aspiration efficiency for mouth inhalation under facing-the-wind condition.

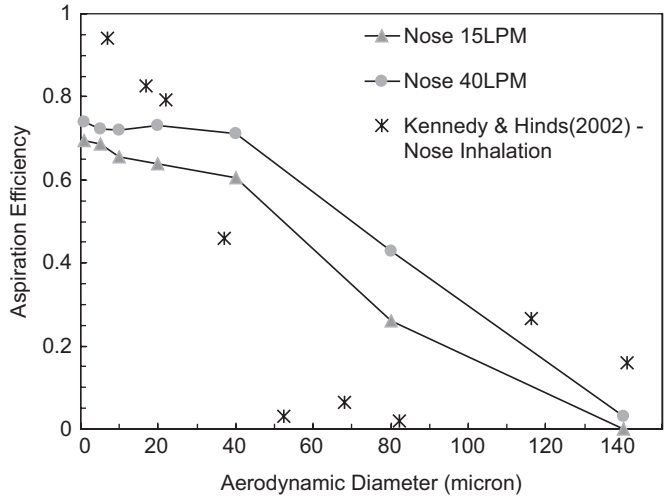

Figure 11. Aspiration efficiency for nasal inhalation under facing-the-wind condition.

manifold approximately 170 cm upstream. This longer distance prevents the larger particles from being transported the entire distance and instead the particles settle to the ground.

Applications

In the design and layout of a workspace, particularly manufacturing, and in a previous case study by the authors (Inthavong et al., 2009), a wood-turning workstation, the location of a contaminant source was not studied. The result from this work is a numerical representation of particles being transported downstream from all locations from a plane. The work was aimed at providing insight into the inhalability of particles under the worst-case scenario to identify the particles and its location that were inhaled, from upstream. The critical area not only identifies the contribution of a particle to the inhalability, but it also provides a means for prevention of particle inhalation. For example, particle sizes between 1 and 20 μm tend to be inhaled below the level of nostrils or mouth, whereas for particles larger than 40 μm, inhalation occurred for particles above the nostrils or mouth. Identifying the inhalability of a particle from a contaminant source provides useful information for allocating aerosol-generating machinery to avoid inhalation of those undesirable aerosols. In addition, lower inhalability may be achieved with nasal breathing. The implication here is that a worker's exertion becomes important when exposed to harmful aerosols. Breathing at normal or low exertion is normally through the nose, whereas heavy exertion leads to oral-nasal breathing and in some cases may even be wholly oral breathing. Under this type of exertion, a worker will be subjected to different levels of exposure to the inhalability of particles. Therefore, when setting the exposure time a worker is allowed to be under, one must consider the type of inhalation that will occur given the type of work that the worker is enduring.

The results from this study also contribute towards a holistic modeling approach through the aspiration efficiency, which can be converted into an inhalable particle size distribution (PSD). This can be calculated by multiplying the particle size distribution by its corresponding aspiration efficiency. From the measured PSD of settled particles by Chung et al. (2000), the inhalable PSDs for pine and oak dust for oral breathing and nasal breathing are given in Figure 12 and Figure 13, respectively. Four additional particle sizes (2, 3, 15, and 24 μm) had been studied to cover more particle sizes for oak dusts. It is found that the inhalable PSD through either the mouth or nostrils generally gives lower values than the experimental PSD. The fraction reduced more significantly about the mean particle size of pine and oak dusts. Because the inhalability has taken into consideration the inhalation rate, wind speed, and dimension of openings, the inhalable PSDs presented can be applied as initial boundary

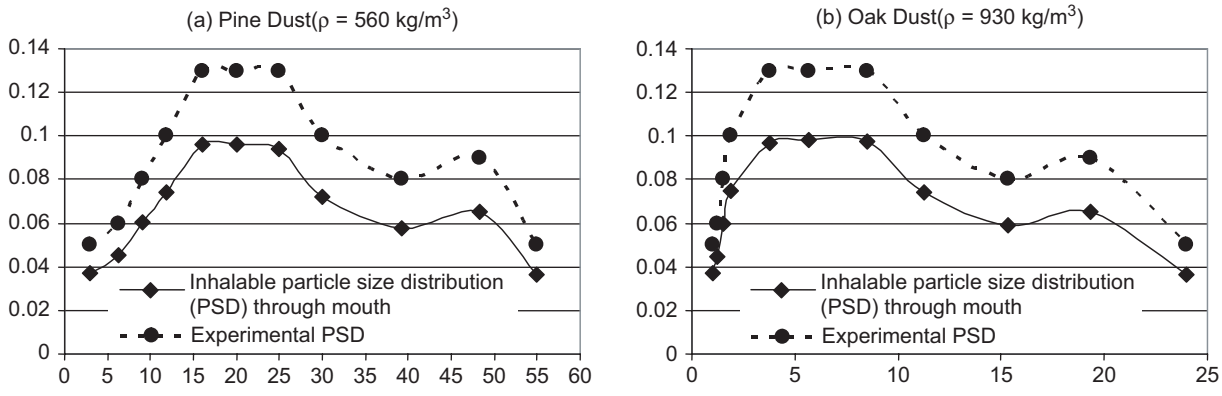

Figure 12. Inhalable particle distribution (PSD) through mouth and ideal PSD for (a) pine and (b) oak dusts.

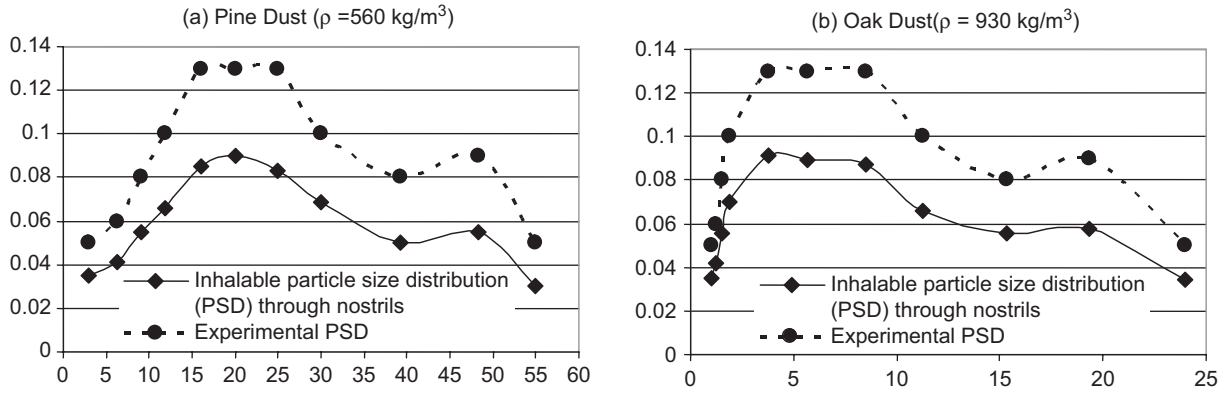

Figure 13. Inhalable particle distribution (PSD) through nostrils and ideal PSD for (a) pine and (b) oak dusts.

conditions for respiratory particle deposition studies. In addition, any normalized PSD using the aerodynamic diameter can be used in conjunction with the aspiration efficiency to provide an inhalable PSD.

Conclusion

Aspiration efficiency through the nostrils and mouth at low velocity environments was investigated using CFD techniques. Particle transport was simulated with a three-dimensional humanoid with detailed facial features. Velocity vectors in the *y-z* plane at the centerline of the humanoid were compared with the experimental data reported by Anthony et al. (2005) to ensure confidence in the results. The flow field in the near breathing region shows slight vertical direction caused by the presence of the torso, where the airstream diverges as it flows past the body. The critical area concept was used as a tool to determine the aspiration efficiency of particles. At any plane normal to the facing mannequin upstream, there exists a region (area) of particles that are inhaled. This region or critical area on a plane is found at varying vertical distance in relation to the mouth. Smaller Stokes number particles that are entrained in the flow exhibit a critical area located at a vertical distance below the mouth due to the flow field vectors directed having an upwards direction. The critical area for larger Stokes number particles is found at a vertical distance higher than the mouth due to gravitational settling. With even heavier particles, the contaminant source location needs to be increasingly higher for the same upstream release distance from the humanoid. Comparisons between critical areas for the nose and mouth inhalations show similar geometric properties such as the teardrop shape, and its vertical distance location on the x-z plane located at y = 70 cm upstream. The critical area sizes were found to be slightly larger for the mouth inhalation, mainly due to the larger mouth area and also the aligned orientation of the mouth to the upstream flow, whereas the nose is perpendicular to the upstream flow. The AE does not change greatly for aerodynamic diameters between 1 and 70 µm, but a large drop in the AE is found for aerodynamic diameters greater than 70 µm. This is in contrast to the established IPM curve, which shows a rapid drop in AE for smaller particles and a plateau for aerodynamic diameters greater than 70 µm. This study's inhalability curve along with those of the Anthony and Flynn (2006b) and Kennedy and Hinds (2002) studies showed significant deviation from the IPM sampling criterion. The source of the difference is unknown, but may be related to differences in experimental/computational set up. The results for the nose data were generated computationally and were compared with one set of experimental results. No other data for nose inhalation exist and it is anticipated that these results can be used for comparisons in future work where transient inhalation conditions can be simulated. This study was undertaken to establish the flow field in the near breathing region, which will help to characterize the flow field and particle field for initial boundary conditions, leading to a more holistic modeling approach of respiration through the nasal cavity and mouth. Refined models to include unsteady flows and different orientations will be further conducted.

Declaration of interest

The findings and conclusions in this report are those of the authors and do not necessarily represent the views of the Australian Research Council and RMIT University. The financial support provided by the Australian Research Council (project ID LP0989452) and by RMIT University through an Emerging Research Grant are gratefully acknowledged.

References

ANSYS. CFX v11. Documentation 11. ANSYS.Inc., USA.

ANSYS. ICEM CFD 11.0.1. ANSYS.Inc., Pennsylvania, USA.

Anthony TR, Flynn MR. 2006a. CFD model for a 3-D inhaling mannequin: Verification and validation. Ann Occup Hyg 50:157–173.

Anthony TR, Flynn MR. 2006b. Computational fluid dynamics investigation of particle inhalability. J Aerosol Sci 37:750–765.

Anthony TR, Flynn MR, Eisner A. 2005. Evaluation of facial features on particle inhalation. Ann Occup Hyg 49:179–193.

Armbruster L, Breuer H. 1982. Investigations into defining inhalable dust. In: Walton WH, ed. Inhaled Particles V. Oxford: Pergamon Press pp. 21–32.

Balashazy, I, Hofmann W, Heistracher T. 2003. Local particle deposition patterns may play a key role in the development of lung cancer. J Appl Physiol 94:1719–1725.

Baldwin, PEJ, Maynard AD. 1993. A survey of wind speeds in indoor workplaces. Ann Occup Hyg 42:303–313.

Bird AJ. 2005. Use of numerical calculations to simulate the sampling efficiency performance of a personal aerosol sampler. Aerosol Sci Technol 39:596–610.

Brohus H. 1997. CFD simulation of personal exposure to contaminant sources in ventilated rooms. Paper read at Proceedings of Ventilation '97, The 5th International Symposium on Ventilation for Contaminant Control, Global Developments in Industrial Ventilation, 14–17 September 1997, at Ottawa, Canada.

Brohus H, Nielsen PV. 1996. CFD models of persons evaluated by full-scale wind channel experiments. Paper read at Proceedings of Roomvent '96, 5th International Conference on Air Distribution in Rooms, 17–19 July 1996, at Yokohama, Japan.

Chung IP, Trinh T, Dunn-Rankin D. 1997. Experimental investigation of a two-dimensional cylindrical sampler. J Aerosol Sci 25:935–955.

Chung KYK, Cuthber RJ, Revell GS, Wassel SG, Summer N. 2000. A study on dust emission, particle size distribution and formaldehyde concentration during machining of medium density fibreboard. Ann Occup Hyg 44:455–466.

Crowder TM, Rosati JA, Schroeter JD, Hickey AJ, Martonen TB. 2002. Fundamental effects of particle morphology on lung delivery: Predictions of Stokes law and the particular relevance to dry powder inhaler formulation and development. Pharm Res 19:239–245.

Dunnet SJ, Ingham DB. 1988. The human head as a blunt aerosol sampler. J Aerosol Sci 19:365–380.

Durbin PA. 1995. Separated flow computations with the k-epsilon-v-squared model. AIAA J 33:659–664.

Erdal S, Esment A. 1995. Human head model as an aerosol sample: Calculation of aspiration efficiencies for coarse particles using an idealised human head model facing the wind. J Aerosol Sci 33:237–255.

Guilmette RA, Cheng YS, Yeh HC, Swift DL. 1994. Deposition of 0.005–12µm monodisperse particles in a computer-milled, MRI-based nasal airway replica. Inhal Toxicol 6(S1):395–399.

Heist DK, Eisner AD, Mitchell W, Wiener R. 2003. Airflow around a child-size manikin in a low-speed wind environment. Aerosol Sci Technol 37:303–314.

Hsu DJ, Swiftt Dl. 1999. The measurements of human inhalability of ultralarge aerosols in calm air using mannikins. J Aerosol Sci 30:1131–1343.

Hyun S, Kleinstreuer C. 2001. Numerical simulation of mixed convection heat and mass transfer in a human inhalation test chamber. Int J Heat Mass Transfer 44:2247–2260.

Ingham DB, Hildyard ML. 1991. The fluid-flow into a blunt aerosol samper oriented at an angle to the oncoming flow. J Aerosol Sci 22:235–252.

Inthavong K. 2006. A numerical study into local deposition sites in the nasal cavity for therapeutic and pollutant inhalation. In: Ansys Australasian Users Conference Proceedings 22–23 November 2006. Melbourne, Australia.

Inthavong K, Tian ZF, Li HF, Tu JY, Yang W, Xue CL, Li CG. 2006. Local deposition sites of drug particles in a human nasal cavity. Paper read at Fifth International Conference on CFD in the Process Industries, 13–15th December, 2006, at Melbourne, Australia.

Inthavong K, Tian ZF, Tu JY. 2009a. Effect of ventilation design on removal of particles in woodturning workstations. Build Environ 44:125–136.

Inthavong K, Tu JY, Ahmadi G. 2009b. Computational modelling of gas-particle flows with different particle morphology in the human nasal cavity. J Comput Multiphase Flows 1(1):57–82.

Inthavong K, Yong Y, Ding S, Tu JY, Subic A, Thien F. 2008a. Comparative study of the effects of acute asthma in relation to a recovered airway tree on airflow patterns. Presented at 13th International Conference on Biomedical Engineering (ICBME2008). Singapore.

Inthavong K, Yong Y, Ding S, Tu JY, Subic A, Thien F. 2008b. Airway geometry and inhalation effort comparisons in a narrowed and recovered airway caused by acute asthma. In: International Conference on Audio, Language and Image Processing 2008 (ICALIP2008, Paper 581). Shanghai, China: IEEE.

Kennedy NJ, Hinds WC. 2002. Inhalability of large solid particles. J Aerosol Sci 33:237–255.

Kleinstreuer C, Zhang Z. 2003. Targeted drug aerosol deposition analysis for a four-generation lung airway model with hemispherical tumours. J Biomech Eng 125:197–206.

Menter FR, Esch T. 2001. Elements of Industrial Heat Transfer Predictions. Paper read at 16th Brazil.an Congress of Mechanical Engineering (COBEM), at Uberlandia, Brazil.

Ogden TL, Birkett JL. 1977. The human head as a dust sampler. In: Walton WH, ed. Inhaled Particles IV. Oxford: Pergamon Press.

Schiller L, Naumann A. 1933. A drag coefficient. Correlation. Z Ver Dtsch Ing 77:318–320.

Shi H, Kleinstreuer C, Zhang Z. 2008. Dilute suspension flow with nanoparticle deposition in a representative nasal airway model. Phys Fluids 20:1–23.

Singularity Inversion, Inc. 2007. FaceGEN Modeller.

Snyer WS, Cook MJ, Nasset ES, Karhausen LR, Parry Howells G, Tipton IH. 1975. Report of the Task Group on Reference Man, International Commission on Radiolofical Protection. Oxford: Pergamon Press.

Speziale CG, Thangam S. 1992. Analysis of an RNG based turbulence model for separated flows. Int J Eng Sci 30:1379–1388.

Tian ZF, Inthavong K, Tu JY. 2007. Deposition of inhaled wood dust in the nasal cavity. Inhal Toxicol 19:1155–1165.

Tilley AR. 1993. The Measure of Man and Woman. New York: The Whitney Library of Design.

Vincent JH, ed. 1999. Particle Size-Selective Sampling for Particulate Air Contaminants. Cincinnati: American Conference of Governmental Industrial Hygienists.

Vincent JH, Mark D. 1982. Application of blunt sampler theory to the definition and measurement of inhalable dust. In: Walton WH, ed. Inhaled Particles V. Oxford: Pergamon Press.

Zhu S, Kato S, Murakami S, Hayashi T. 2005. Study on inhalation region by means of CFD analysis and experiment. Build Environ 40:1329–1336.

Zwartz GJ, Guilmette RA. 2001. Effect of flow rate on particle deposition in a replica of a human nasal airway. Inhal Toxicol 13:109–127.